Fluorescent molecular rotors

From working principles to visualization of mechanical contacts

Suhina, T.

1 Introduction

1.1 Real contact area

1.1.1 Real and apparent contact area

The goal of this project was to develop and characterize methods that enable direct visualization of the real contact area between solid objects. The real contact area is more often than not significantly different from the apparent contact area that we perceive macroscopically. This is illustrated in Fig. 1.1 a), where we show a cartoon of an apparently smooth object lying on a flat, and apparently smooth substrate. The contact area we would macroscopically observe between such objects would resemble the one shown in Fig. 1.1 b). If, however, we would image both surfaces by atomic force microscopy (or some other appropriate method), we would observe that our initial assumption about the smoothness of the surfaces was incorrect for either of the two objects. The surface of any real object consists of hills and valleys that are commonly referred to as asperities (Fig. 1.1 a)). The real contact area between the touching objects, then, is not the contact area that we perceive macroscopically (Fig. 1.1 b)), but the area of contact that is formed between the asperities on the surfaces of the objects in contact (see Fig. 1.1 a) and c)). Visualization of microscopic contacts between objects is, however, challenging to do experimentally. Atomic force microscopy, for example, provides resolution that is sufficient to detect and measure roughness of most materials, but it is inherently unable to image contacts *between* macroscopic objects.[1] When touching objects are transparent, the contact area between them can, in principle, be imaged by looking at the interference pattern of light that is reflected by both surfaces.[2] Interference-based contact imaging methods have, however, limited ability to distinguish contacts from non-contacts in experimental situations such as the geometries examined in this thesis (Chapters 7 and 8), and presumably, many others.

Our motivation to visualize contacts on such small scales comes from the fact

that real contact area is closely related to friction:[1,3,4] a force that resists relative motion between objects that are in mutual contact.[3] Examples where friction plays an important role can be found everywhere: from cars or bikes in the street, trains, airplanes, people having a walk, et cetera. One can imagine many examples where friction is useful. If there was no friction we couldn't walk or drive. Without friction playing ice hockey and musical instruments would not be possible. But in many cases, we would like to minimize its influence. For example, an average car uses only 21.5 %[5] of the fuel to perform useful work (moving the car). The rest of the energy is "wasted" on overcoming friction. In this example, friction not only causes environmental damage, but also costs a lot of money. The wasted energy in our cars is, however, only a small fraction of the total energy losses where friction plays an important role. It is estimated that around 30 % of the world's energy consumption is due to friction.[6]

1.1.2 A brief historical look on friction and its relation to the (real) contact area

Friction is truly a subject of immense importance. It is, therefore, no wonder that the human race has been trying to manipulate friction one way or another for more than 400 000 years.[7–11] The earliest documented example of a systematic research conducted on friction dates all the way back to the 15th century: Leonardo da Vinci.[11] Da Vinci made two important observations. The first one was that the frictional force F_{FR} is directly proportional to the applied load L. In other words, if he would double the weight of the object he was trying to move, he would also need to double the invested force F (see Scheme 1.1 a)) in order to move it. His second observation was that frictional force remained the same, no matter which way he turned the object relative to the surface (Scheme 1.1 b)). Because of this, he concluded that the frictional force is independent of the (macroscopic) contact area between the sliding objects.

These observations were confirmed by Amontons (17th-18th century) and are since then referred to as Amontons first and second law of friction.[12] The proportionality factor between load and frictional force is given by μ, the friction coefficient (see Eqs. 1.1 and 1.2). This coefficient assumes different values if the object is at rest (static friction coefficient, μ_s) or is already moving (dynamic fric-

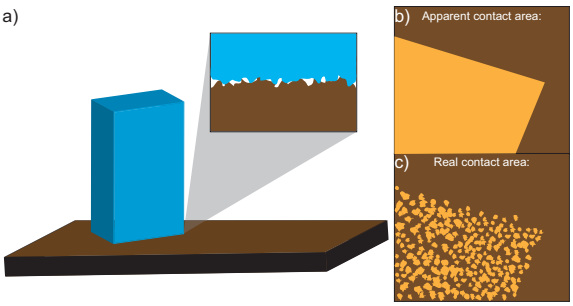

Figure 1.1: a) Illustration of the apparent and the real contact area which is formed between two surfaces. Due to the inherent material roughness, real contact area differs from the apparent contact area; b) the macroscopically perceived apparent area of contact; c) real contact area.

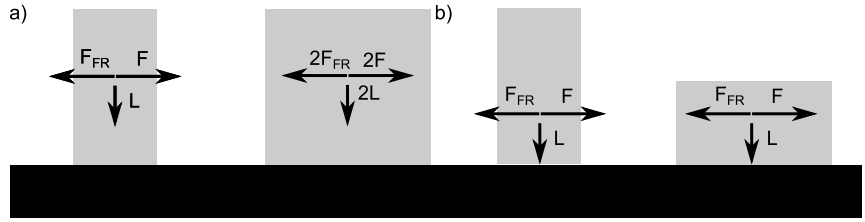

Scheme 1.1: Schematic representation of Leonardo da Vinci's experimental observations: a) if the load is doubled, the force needed to move the object doubles as well; b) the force needed to move the object remains the same no matter how the object is positioned relative to the surface.

tion coefficient, μ_k). In the 18th century, Coulomb observed that the frictional force does not change with the sliding velocity v and this observation came to be known as the third law of friction.[13] The three laws of friction can be mathematically expressed by Eq. 1.1. Although this expression is known not to be valid for certain situations (especially if adhesion forces are present[14,15]), it describes the majority of situations rather well.[1] Even today, this equation is in wide-spread use, and the values of μ can be found tabulated in textbooks and handbooks.

$$\mu_s = \frac{\vec{F}_{fr}}{\vec{L}}, \text{ (if } v = 0)) \tag{1.1}$$

$$\mu_k = \frac{\vec{F}_{fr}}{\vec{L}}, \text{ (if } v \neq 0)) \tag{1.2}$$

In spite of the fact that Eqs. 1.1 and 1.2 do not consider the area of contact between objects, our everyday experience points to a different conclusion. One example that comes to mind is when we rub our hands together in order to warm them during a cold winter day. As long as our palms are in contact we experience resistance as we slide one palm over another, and this generates heat. If we separate our palms and keep moving them relative to one another, we experience no resistance and generate no heat. Racing cars are equipped with wide tires to maximize the area of contact with the road. Lubricating oils that we use in engines create a film between surfaces and prevent them from coming into a direct contact. Numerous examples similar to these could be given, because friction occurs only between objects that are in contact and shows contact area dependence. It may therefore be somewhat surprising to find Eq. 1.1, which does not take the contact area between the two touching surfaces into account, in such a wide-spread use today. This is because Eq. 1.1 simplifies (and generalizes) a very complex phenomenon, in which the meaning of μ is not well understood.[4] In a real world, perfectly smooth surfaces do not exist: every surface consists of hills and valleys that are called asperities. The contact area between touching surfaces, then, is not the macroscopic contact area observed by da Vinci and Amontons, but the area of real contact between the asperities present on each of the surfaces (see Fig. 1.1).

The relation between friction and a real contact area is the topic of a considerable research interest.[1–4,16,17]

Bowden and Tabor considered the connection between the real contact area and friction in their, now classic, work from 1939.[18] The authors measured the current between two metal cylinders and devised a relation between the electrical conductivity and the real contact area. They observed that the electrical conductivity at the interface was proportional to the exerted load upon pressing two metal surfaces together, which led them to conclude that asperities undergo a plastic (irreversible) deformation (meaning that $A \propto L$). Because the lateral force needed to plastically deform the asperity junction is proportional to the area of the junction, they directly arrived to Eq. 1.1. The observation that asperities undergo plastic deformation was, however, not in agreement with the widely accepted contact theory developed by Hertz[19] in 1881, according to which $A \propto (RL)^{2/3}$ for a sphere of radius R pressed on a flat surface. This theory assumes that strains within the contact zone are small and within the elastic limits of materials that form contact. Since Hertz contact mechanics was so successful to predict contact area for a huge number of macroscopic cases (it is still widely used today), it is no wonder that Bowden and Tabor's conclusion about purely plastic contact junctions caused some stir within the community.[20,21] This led to development of the so-called multi-asperity contact theory by Archard. This theory assumes that surface roughness can be approximated by asperities of varying heights with spherical tips that undergo Hertzian (elastic) deformation, and predicts a linear dependence of frictional force on load.[20–23] Another notable work that should be mentioned was done by Persson, whose relatively recent theory of rough contacts mechanics offers a significant improvement over the multi-asperity theories.[24]

The theories I have mentioned so far represent only a fraction of theoretical and experimental work that was done in this field (see refs. 1,4,15 and refs. therein), and their individual considerations (even in the most simplified form) are beyond the scope of this short overview. In spite of the immense effort invested in understanding the relation between contact area and friction, a direct, convenient and sufficiently flexible experimental method for dynamic contact visualization is lacking. Development and characterization of such a method is the topic of this thesis.

1.2 Fluorescent molecular rotors

1.2.1 What are fluorescent molecular rotors?

Fluorescent molecular rotors belong to a special class of fluorescent probes which gained popularity as viscosity sensors due to the pronounced sensitivity of their fluorescence quantum yields (Φ_f) on the viscosity (η) of their immediate environment.[25,26] Some typically used fluorescent molecular rotors are shown in Scheme 1.2. These molecules are very weakly fluorescent in low viscosity solvents, but as their environment becomes more viscous, their fluorescence quantum yields show a remarkable increase. Weak fluorescence in low viscosity media comes from their

tendency to undergo a large amplitude geometrical distortion in the fluorescent excited state that results in fluorescence quenching.[25,27–29] The quenching process either proceeds through direct ground state repopulation[29] (via a conical intersection taking place between the ground and the excited state potential energy surfaces) or through the intermediate twisted intramolecular charge transfer (TICT) state[30], formation of which either results in dual emission (as in dimethylamino benzonitrile)[30,31] or a dark intermediate state.

1.2.2 Applications of confinement sensitive molecules

Fluorescent molecular rotors gained a significant popularity as probes for measuring viscosity and free volume since their discovery. Out of the large number of examples available in literature, only a few selected ones will be mentioned below.

Biological applications. A common example of molecular rotor used in biology on a routine basis is Thioflavin T (see Scheme 1.2).[34] Its fluorescence response towards viscosity changes is shown in Fig. 1.2 a). Because Thioflavin binds to amyloid fibers, upon which intermolecular motion becomes severely restricted, this rotor is nowadays routinely used to study protein aggregation and fibril formation.[33,35–37] One example, in which the authors quantify the amount of amyloid fibril structure is shown in Fig. 1.2 b).[33] Because of selective binding of Thioflavin to β amyloid fibril (β(1-28) in this case), the fluorescence of the former increases as the concentration of the peptide increases. This way, the fluorescence response of the calibrated system can be used to quantify the amount of fibril in the sample.[33] The usability of other molecular rotors in studying protein aggre-

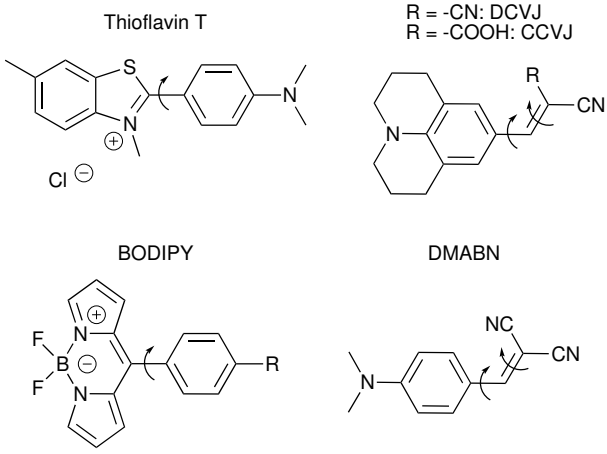

Scheme 1.2: Molecular structures of fluorescent molecular rotors that are routinely used as viscosity sensors. Arrows indicate the main reaction coordinates that have been proposed to result in fluorescence quenching.

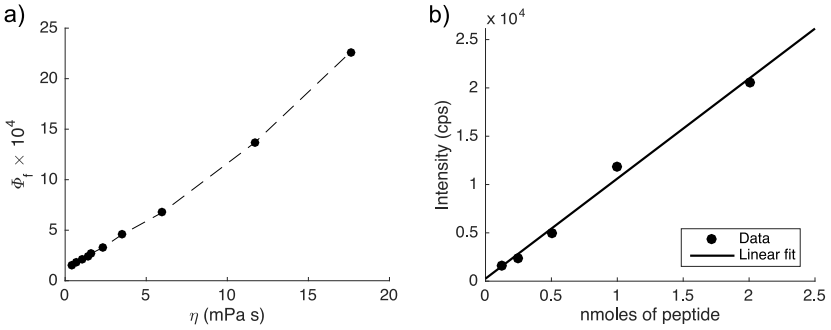

Figure 1.2: a) Fluorescence quantum yield of Thioflavin T in acetonitrile/Ethylene glycol mixtures as a function of environment viscosity (from ref. 32); b) Quantification of β(1-28) amyloid fibril in 50 mM phosphate buffer (pH = 6) based on the turning of the fluorescence of Thioflavin T, data from ref. 33.

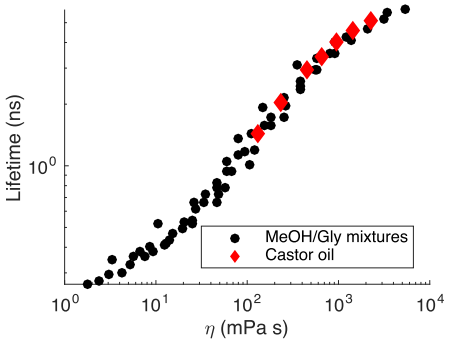

Figure 1.3: Fluorescence lifetime *vs* viscosity calibration curves of a BODIPY-based molecular rotor obtained in MeOH/glycerol mixtures (circles) and Castor oil between 10 °C and 60 °C, used in determining the viscosity of lipid membranes. Data from ref. 40.

gation has also been demonstrated. Kung and Reed, for example, have used the fluorescence response of DCVJ to monitor tubulin aggregation and assembly.[38] The applicability of molecular rotors towards probing specific peptide-protein interactions is being actively developed, and offers the possibility to improve on the existing high-throughput drug-screening procedures.[39]

Since fluorescent molecular rotors often react to changes in viscosity in a predictable manner, their response can be calibrated, and used to measure the viscosity of samples for which conventional viscosity measurements are difficult to conduct.[40–42] For example, Dent *et al.* indirectly measured the viscosity in model lipid membranes by calibrating the fluorescence response of a BODIPY-based molecular rotor to viscosity changes in polar and non-polar environments (see Fig. 1.3). BODIPY-based molecular rotors have also been used for viscosity measurements in live cells, as their red shifted absorption and emission spectra make them suitable for use in fluorescence microscopy experiments.[43]

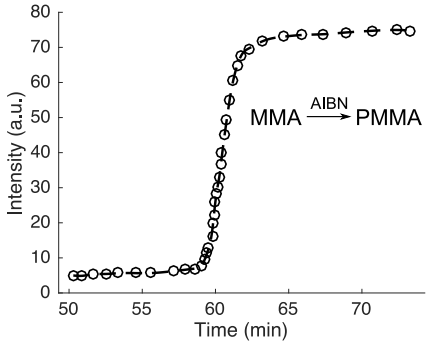

Figure 1.4: Polymerization of methyl methacrylate (MMA) monitored by the fluoresence response of the DCVJ molecular rotor. Data from ref. 44.

Applications in Material and Polymer Science. In addition to bulk viscosity measurement of liquids,[41,45] molecular rotors have been used as probes in polymer research. Loutfy used DCVJ and analogous probes to monitor polymerization of PMMA, as shown in Fig. 1.4.[44] Loutfy argued that a polymerization reaction decreases the free volume available for the probe to undergo the intramolecular motion that results in nonradiative relaxation.[44] Royal and Torkelson used DCVJ to study molecular scale relaxations (polymer aging) in a series of polymer matrices.[46,47] Zhu *et al.* demonstrated that a CCVJ derivative can be used to monitor chain entanglement in poly(propylene oxide) melts, further supporting assumptions about free-volume sensing capabilities of fluorescent molecular rotors.[48]

1.2.3 The role of fluorescent molecular rotors in contact area imaging

In this section, I will attempt to provide some context for using molecular rotors in the experiments described in this thesis. As mentioned at the end of Section 1.1.2, our goal was to develop a reliable method that would help us in understanding the role of the real contact area between touching surfaces in friction. In order to do this, our method of choice had to not only provide us with information about the size of contacts between surfaces, but also about information about the shape of the contact area and the changes it undergoes during sliding and aging processes. This consideration pointed us towards surface imaging techniques. Although arguably a number of techniques capable of performing high resolution surface imaging exist (atomic force microscopy, scanning tunneling microscopy, fluorescence/reflections imaging, high resolution scanning electron microscopy, high resolution transmission electron microscopy...), only a very limited number of techniques make it possible to look at the contacts between surfaces directly and with sufficient spatial and temporal resolution. In order to tackle this problem we chose fluorescence microscopy to visualize contacts, because of its ability to look at contact area directly (if at least one of the surfaces is transparent), and it offers

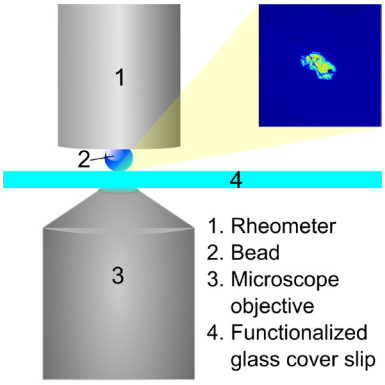

Figure 1.5: Illustration of contact imaging experiment and a typical fluorescence image with molecular rigidochromic probes.

excellent sensitivity, speed and is nowadays easily accessible and more versatile than alternative methods.

The fluorescence microscopy setup used in contact imaging is shown in Fig. 1.5. Our goal was to press a relatively rough object onto a smooth surface with a controlled load, and to monitor how the contact area behaves as the bead is pressed on (or moved around) the surface. Since the main criterion for our method to be successful was its ability to clearly differentiate very small contact points from background, such experiments required signal reporters to be very small and efficient. For this purpose, fluorescent molecular rotors seemed as an optimal choice. We approached the problem by covalently attaching molecular rotors designed in our lab onto one of the surfaces. We envisioned that surface immobilization by itself would not significantly hinder the large-amplitude geometrical distortions that result in excited-state deactivation of molecular rotors, and they would behave as in low-viscosity solvents. Once confined by another surface (bead), however, intramolecular motions that are responsible for fluorescence quenching would become significantly hindered at contact points, and this would result in strong fluorescence that would be imaged by fluorescence microscopy. The validity of this approach is demonstrated in Chapters 3, 7, and 8 of this Thesis.

1.2.4 Why DCDHF-based molecular rotors?

For the purpose of this project, we searched for molecular probes that would provide the strongest response towards surface-induced confinement.
Dicyanomethylenedihydrofuran-based (DCDHF) molecular rotors turned out to be optimal probes for imaging contact-induced surface confinement, as they offer a number of advantages over other (more commonly used) functionally similar molecules mentioned above: low-energy absorption/emission spectra, reasonable Stokes shifts, remarkable photostability, and synthetic tunability.

In this section, we will provide a brief overview of DCDHF molecular rotors and explain their benefits over other molecular rotors, as a large part of the work described in this thesis is based on their unique properties. DCDHF-based chro-

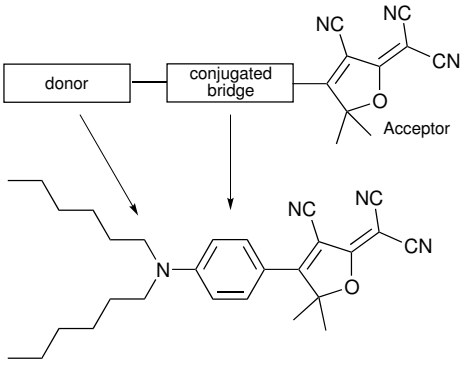

Scheme 1.3: Schematic representation of DCDHF-based molecular rotors.

mophores were initially developed for non-linear optics applications.[49–52] The general structure of these molecules is shown in Scheme 1.3. They consist of electron donor (usually aniline), π-conjugated bridge and DCDHF acceptor units. This design was initially meant to enhance their polarizability anisotropy, an important material property for enhancing the photorefractive effect.[49] As expected for donor-acceptor systems, fluorescence quantum yields of these molecules were found to be very low in room temperature solvents, but it was soon shown that their fluorescence is dramatically enhanced in rigid polymer matrices.[53] Such behavior indicated that large-amplitude intramolecular motions play a role in fluorescence deactivation of these compounds, and it was proposed that they behave as previously reported fluorescent molecular rotors.[27]

DCDHF molecular rotors, due to their pronounced charge-transfer character, exhibit solvatochromic behavior: their absorption and emission spectra show a pronounced shift in response to environment polarity.[54] This property is very useful in applications which aim to examine the polarity of a chromophore's environment.[26] As with most push-pull systems, molecular dipole moments of these compounds increase significantly upon photoexcitation.[54,55] This results in additional stabilization of the excited state relative to the ground state, which results in increasingly larger differences between the excitation and emission energies (Stokes shifts) as the environment polarity increases.[26,54] The influence of solvent polarity on the exhibited Stokes shifts is commonly expressed by the Lippert-Mataga equation:

$$\nu_{\mathrm{abs}} - \nu_{\mathrm{em}} = \frac{2}{hc}\Delta f \frac{(\vec{\mu}_{\mathrm{ES}} - \vec{\mu}_{\mathrm{GS}})^2}{a^3} + constant, \tag{1.3}$$

where ν_{abs} and ν_{em} represent the absorption and emission energies (in cm^{-1}), h and c are Planck's constant and the speed of light in vacuum, $\vec{\mu}_{\mathrm{GS}}$ and $\vec{\mu}_{\mathrm{ES}}$ are the ground-state and excited-state dipole moments, and a is the solvent cavity

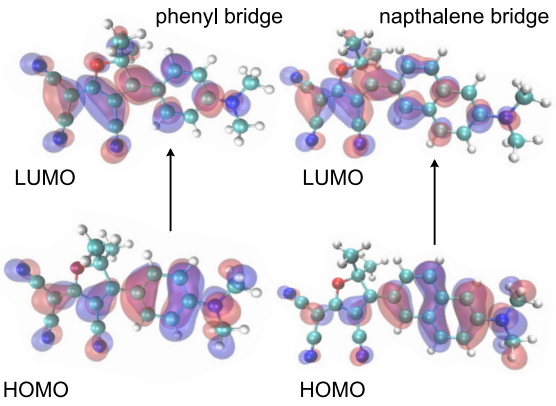

Figure 1.6: Frontier molecular orbitals (HF-3c[56] geometries optimized in Orca[57]) of DCDHF molecular rotors with phenyl (left) and napthalene (right) bridge units (visualized with VMD[58]).

radius. Δf is a solvent orientational polarization function, which is defined as:

$$\Delta f = f(\epsilon) - f(n^2) = \frac{\epsilon - 1}{2\epsilon + 1} - \frac{n^2 - 1}{2n + 1}, \tag{1.4}$$

where ϵ represents the relative dielectric permittivity and n the refractive index of the medium. While $\Delta f(\epsilon)$ takes into account the full dielectric response of the solvent (fast electronic polarization and slow molecular reorientation in the field of the solute dipole), Δf takes only the "slow" molecular reorientation into account.

It is expected that increasing the conjugation length would result in larger $\mu_{ES} - \mu_{\mathrm{GS}}$ and increased sensitivity of Stokes shifts towards solvent polarity. As an example, we illustrate this by replacing the phenyl bridge unit with naphthalene, and optimize geometries of these molecules. Such substitution results in enhanced charge migration and distance over which charge migration takes place, as indicated by the frontier orbitals shown in Fig. 1.6. This results in a larger difference between the ground-state and excited-state dipole moments, which manifests itself in larger Stokes shifts. Experimental findings have indeed shown that both absorption/emission energies, and Stokes shifts can be tuned by synthetic modifications illustrated in Fig. 1.7, where phenyl unit (compound **1**) gets replaced by napthalene (compound **2**) and anthracene (compound **3**).[54] Low-energy excitations/emissions and large Stokes shifts are highly desirable molecular properties when considering the potential use of these molecules in fluorescence microscopy applications. This is because the background fluorescence significantly decreases at lower excitation energies, and because the excitation light can be separated from the emitted light more efficiently when absorption and emission spectra are well separated (large Stokes shifts). It was, however, reported that an increased level of conjugation obtained by using acene groups results in much higher fluorescence quantum yields of DCDHF derivatives **2** and **3** relative to **1** in toluene. For example, fluorescence quantum yields of **2** and **3** shown in Fig. 1.7 ($\Phi_{\mathrm{f}} > 0.5$) in toluene are more than an order of magnitude higher than fluorescence quantum yields reported for compound **1** ($\Phi_{\mathrm{f}} = 0.043$).[54] This would, in principle,

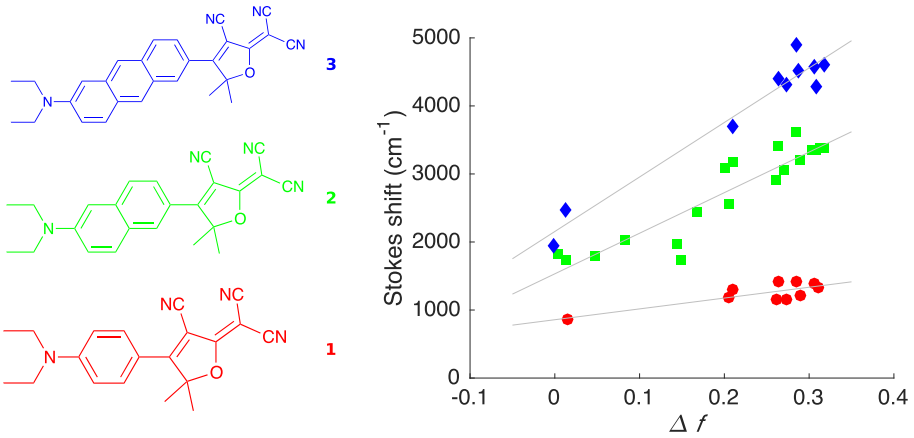

Figure 1.7: Solvatochromic response of DCDHF molecular rotors with different bridge units. Data from ref.[54].

make such molecules rather inconvenient for contact imaging purposes (at least in non-polar environment), because the contrast between the confined and the unconfined probes would be rather poor. In a polar environment, however, fluorescence quantum yields of compounds **2** and **3** drop below 3 %.[59] Although the reason behind such a large difference in fluorescence quantum yields between polar and non-polar environments was not clear when this project started, the reported quantum yields from ref. 59 suggest that the model for excited-state deactivation that we propose in Chapters 4 and 5 for the phenyl-bridged derivative **1** is able to explain the quantum yield trends of the DCDHF acenes in different solvents. A similar approach towards extending the degree of conjugation was made by using oligoaromatic building blocks (by combining vinly, phenyl, thiophene π-conjugated bridges),[60] and this is the approach that we use in Chapter 7 to design and prepare a red-shifted, phenyl-vinyl-bridged DCDHF analogue that shows excellent sensitivity towards contact-induced confinement.

1.2.5 Origin of sensitivity towards molecular confinement

Because fluorescent molecular rotors need to perform large intramolecular distortions (see Scheme 1.2 where relevant torsions are indicated by arrows) in order for fluorescence deactivation to take place,[29,61–64] increasing η hinders such movement and results in pronounced increase of Φ_f.[27,28,44,62] Correlation between fluorescence quantum yield and η is commonly quantified in terms of the Förster-Hoffmann equation (Eq. 1.5):[65]

$$\Phi_f = z\eta^{\alpha}, \tag{1.5}$$

where z represents a dye-dependent constant and α is a constant which describes how well changes in fluorescence quantum yields correlate with bulk viscosity of the environment. Förster and Hoffmann derived this expression by a

theoretical treatment based on Debye-Stokes-Einstein (DSE) diffusion theory and obtained the value of $\alpha = 2/3$.[65] A number of workers, however, report varying values of α even for the same molecular rotors in different solvent systems (see refs. 66 and 48 for some amongst many examples that can be found in literature). This discrepancy can be (at least qualitatively) explained by the fact that molecular rotors do not show sensitivity towards the bulk viscosity, but towards the microviscosity of their immediate environment.[25,27,31,66,67] Molecular rotors are comparable in size to solvent molecules, so one can expect that the relative size of molecular rotor and solvent cavities influences α. Law took a somewhat more flexible approach[27] in order to arrive to Eq. 1.5. Law started by assuming that viscosity of a liquid depends on the ratio between the molecular (van der Waals) volume (V_0) and the free volume (V_f) of the solvent, as was previously formulated by Doolittle:[68]

$$\eta = A \exp(\beta \frac{V_0}{V_\mathrm{f}}), \tag{1.6}$$

where A and β represent system specific constants. Since it was experimentally shown that fluorescence quenching of molecular rotors similar to DCVJ and DMABN (Scheme 1.2) is viscosity (and free volume) dependent, Law related the quenching rate (k_nr) to free volume via Eq. 1.7. In this expression, γ is a constant, V_0 is the van der Waals volume of the molecular rotor and V_f is the free volume. By assuming that the fluorescence quenching process is irreversible and highly efficient, Φ_f can be expressed as $\Phi_\mathrm{f} = k_\mathrm{rad}/k_\mathrm{nr}$, in which k_rad represents the radiative decay rate of molecular rotor. Inserting Eq. 1.7 into this expression, and expressing V_0/V_f through Eq. 1.6, after some rearrangement and substitution of the constant terms with C, yields Eq. 1.8. This equation is analogous to the commonly used expression attributed to Förster and Hoffmann in Eq. 1.5. At this point, the physical meaning of the parameter α and its interpretation should be mentioned.

$$k_\mathrm{nr} = k_\mathrm{nr0} \exp(-\gamma \frac{V_0}{V_\mathrm{f}}) \tag{1.7}$$

$$\Phi_\mathrm{f} = C\eta^\alpha \tag{1.8}$$

$$\tau_\mathrm{or} = C_\mathrm{RF}\, \eta^\alpha / T \tag{1.9}$$

If we take a close look at Eqs. 1.5 and 1.8, their direct comparison with the famous Debye-Stokes-Einstein diffusion equation (Eq. 1.9, α=1) is difficult to avoid. The DSE equation relates the orientational relaxation time of the particle (τ_{or}) with shear viscosity (η), temperature (T) and rotational friction coefficient of the particle (C_RF). One can see that the physical meaning of α is nothing else than a simple correlation coefficient between the fluorescence ($\Phi_f \propto \tau_{or} \propto 1/k_{nr}$) and bulk viscosity ($\alpha = 1$ for macroscopic objects, $\alpha < 1$ for molecular rotors), and Eq. 1.9 becomes analogous to Eq. 1.8 at a constant temperature.

Purely hydrodynamic approaches (and other interpretations mentioned above) view excite-state decays of molecular rotors as barrierless processes that are exclusively governed by steric constraints imposed by the surrounding environment.

This is not always the case, because excited-state decays of fluorescent molecular rotors often occur on much longer time scales than predicted by hydrodynamic theory and show dependence on solvent polarity.[66,69–71] Even for the commonly used DCVJ, this effect might be significant when changes in environment polarity take place, as suggested in ref. 66 and our preliminary results described in the Appendix to Chapter 5.

In order to account for the presence of an energy barrier, the hydrodynamic equation needs to be modified:

$$k_{\mathrm{nr}}/T = C\ \eta^{\alpha}\ \exp(\frac{-E_{\mathrm{a}}}{RT}), \tag{1.10}$$

where E_{a} represents the energy barrier leading to fluorescence deactivation, R is the gas constant, and T the temperature.[72] The effect of the energy barrier E_{a} and its dependence on solvent polarity is in most cases difficult to quantify.

1.3 Outline and scope of the thesis

This thesis describes experimental and computational research on fluorescent molecular rotors and their use as a tool for studying contact mechanics and friction. In chapter 2, we discuss the experimental methods and data analysis used throughout this thesis. A molecular rotor which based on the DCDHF acceptor unit (compound **1**, Fig. 1.7) and its use in contact area measurements is presented and discussed in Chapter 3. This chapter also serves as a motivation for the following two chapters, in which we discuss the photophysical behavior of this molecule. In Chapter 4, we propose the excited state deactivation pathways for the molecular rotor **1** based on time-resolved fluorescence, femtosecond transient infra-red data and TD-DFT calculations. In Chapter 5, we take a closer look at the solvent polarity-dependent behavior of this molecule with the help of visible-pump/visible-probe and steady-state techniques. In the following chapter (Chapter 6) we present a detailed photophysical study of a molecular rotor based on the unhindered BODIPY core. In Chapter 7 we introduce a new DCDHF-based molecular rotor with increased level of conjugation, which manifests itself in the electronic absorption and emission spectra shifted towards significantly lower energies. We also attempt to use BODIPY-based molecular rotor in contact imaging experiments, but without success. We compare the photophysical behavior of the three molecular rotors discussed so far, take a closer look on their behavior while being confined within the contact zone, and discuss the reason behind the apparent lack of sensitivity towards contact induced confinement of BODIPY-based molecular rotor. Chapter 8 serves as a closing chapter, where we demonstrate the applicability of our method to learning more about contact mechanics and friction.

References

1. Gao, J.; Luedtke, W.; Gourdon, D.; Ruths, M.; Israelachvili, J.; Landman, U. *J. Phys. Chem. B* **2004**, *108*, 3410–3425.
2. Rubinstein, S. M.; Cohen, G.; Fineberg, J. *Nature* **2004**, *430*, 1005–1009.
3. Young, H. D.; Freedman, R. A. *Sears and Zemansky's University Physics*; Addison-Wesley, 2008.
4. Carbone, G.; Bottiglione, F. *J. Mech. Phys. Solids* **2008**, *56*, 2555–2572.
5. Holmberg, K.; Andersson, P.; Erdemir, A. *Tribol. Int.* **2012**, *47*, 221–234.
6. Szeri, A. Z. *Tribology: friction, lubrication, and wear*; McGraw-Hill, 1980.
7. Pursell, C. W.; Kranzberg, M. *Technology in Western Civilization*; JSTOR, 1967.
8. Derry, T. K.; Williams, T. I. *A short history of technology from the earliest times to AD 1900*; Courier Corporation, 1960; Vol. 231.
9. Edwards, J. F. *Technol. Cult.* **2003**, *44*, 340–354.
10. Childe, V. G. *J. Roy. Anthropol. Inst.* **1944**, *74*, 7–24.
11. Dowson, D. *History of tribology*; Addison-Wesley Longman Limited, 1979.
12. Amontons, G. *De la resistance causée dans les machines*; Mem. l'Académie R. A, 1699.
13. Coulomb, C. *Bachelier* **1821**,
14. Yoshizawa, H.; Chen, Y. L.; Israelachvili, J. *J. Phys. Chem.* **1993**, *97*, 4128–4140.
15. Persson, B.; Tosatti, E. *Physics of sliding friction*; Springer Science & Business Media, 1996; Vol. 311.
16. Rubinstein, S. M.; Shay, M.; Cohen, G.; Fineberg, J. *Int. J. Fract.* **2006**, *140*, 201–212.
17. Ben-David, O.; Cohen, G.; Fineberg, J. *Science* **2010**, *330*, 211–214.
18. Bowden, F.; Tabor, D. *Proc. R. Soc. A* **1939**, 391–413.
19. Hertz, H. *J. Reine Angew. Math.* **1881**, *92*, 156–171.
20. Archard, J. *J. Appl. Phys.* **1953**, *24*, 981–988.
21. Archard, J. *Proc. R. Soc. A* **1957**, *243*, 190–205.
22. Archard, J. *Nature* **1953**, *172*, 918–919.
23. Archard, J.; Hirst, W. *Proc. R. Soc. A* **1956**, *236*, 397–410.
24. Persson, B. N. *J. Chem. Phys.* **2001**, *115*, 3840–3861.
25. Haidekker, M. A.; Theodorakis, E. A. *J. Biol. Eng.* **2010**, *4*, 1.
26. Lakowicz, J. R. *Principles of Fluorescence Spectroscopy*; Springer Science & Business Media, 2006.
27. Law, K. *Chem. Phys. Lett.* **1980**, *75*, 545–549.
28. Loutfy, R. O.; Arnold, B. A. *J. Phys. Chem.* **1982**, *86*, 4205–4211.
29. Swalina, C.; Maroncelli, M. *J. Phys. Chem. C* **2009**, *114*, 5602–5610.

30. Grabowski, Z. R.; Rotkiewicz, K.; Rettig, W. *Chem. Rev.* **2003**, *103*, 3899–4032.
31. Rettig, W. *J. Phys. Chem.* **1982**, *86*, 1970–1976.
32. Singh, P. K.; Kumbhakar, M.; Pal, H.; Nath, S. *J. Phys. Chem. B* **2010**, *114*, 5920–5927.
33. LeVine, H. *Methods Enzymol.* **1999**, *309*, 274–284.
34. Naiki, H.; Higuchi, K.; Hosokawa, M.; Takeda, T. *Analytical biochemistry* **1989**, *177*, 244–249.
35. Vassar, P. S.; Culling, C. *Arch. Pathol.* **1959**, *68*, 487.
36. Ban, T.; Hamada, D.; Hasegawa, K.; Naiki, H.; Goto, Y. *J. Biol. Chem.* **2003**, *278*, 16462–16465.
37. Khurana, R.; Coleman, C.; Ionescu-Zanetti, C.; Carter, S. A.; Krishna, V.; Grover, R. K.; Roy, R.; Singh, S. *J. Struct. Biol.* **2005**, *151*, 229–238.
38. Kung, C. E.; Reed, J. K. *Biochemistry* **1989**, *28*, 6678–6686.
39. Goh, W. L.; Lee, M. Y.; Joseph, T. L.; Quah, S. T.; Brown, C. J.; Verma, C.; Brenner, S.; Ghadessy, F. J.; Teo, Y. N. *J. Am. Chem. Soc.* **2014**, *136*, 6159–6162.
40. Dent, M. R.; López-Duarte, I.; Dickson, C. J.; Geoghegan, N. D.; Cooper, J. M.; Gould, I. R.; Krams, R.; Bull, J. A.; Brooks, N. J.; Kuimova, M. K. *Phys. Chem. Chem. Phys.* **2015**, *17*, 18393–18402.
41. Akers, W. J.; Haidekker, M. A. *J. Biomech. Eng.* **2005**, *127*, 450–454.
42. Haidekker, M.; Brady, T.; Lichlyter, D.; Theodorakis, E. *Bioorg. Chem.* **2005**, *33*, 415–425.
43. López-Duarte, I.; Vu, T. T.; Izquierdo, M. A.; Bull, J. A.; Kuimova, M. K. *Chem. Comm.* **2014**, *50*, 5282–5284.
44. Loutfy, R. O. *Macromolecules* **1981**, *14*, 270–275.
45. Levitt, J. A.; Chung, P.-H.; Kuimova, M. K.; Yahioglu, G.; Wang, Y.; Qu, J.; Suhling, K. *ChemPhysChem* **2011**, *12*, 662–672.
46. Royal, J. S.; Torkelson, J. M. *Macromolecules* **1993**, *26*, 5331–5335.
47. Royal, J. S.; Torkelson, J. M. *Macromolecules* **1990**, *23*, 3536–3538.
48. Zhu, D.; Haidekker, M. A.; Lee, J.-S.; Won, Y.-Y.; Lee, J. C.-M. *Macromolecules* **2007**, *40*, 7730–7732.
49. Wright, D.; Gubler, U.; Roh, Y.; Moerner, W.; He, M.; Twieg, R. J. *Appl. Phys. Lett.* **2001**, *79*, 4274–4276.
50. Gubler, U.; He, M.; Wright, D.; Roh, Y.; Twieg, R.; Moerner, W. *Adv. Mater.* **2002**, *14*, 313–317.
51. Ostroverkhova, O.; Wright, D.; Gubler, U.; Moerner, W.; He, M.; Sastre-Santos, A.; Twieg, R. *Adv. Funct. Mater.* **2002**, *12*, 621–629.
52. Ostroverkhova, O.; Moerner, W. *Chem. Rev.* **2004**, *104*, 3267–3314.
53. Willets, K. A.; Ostroverkhova, O.; He, M.; Twieg, R. J.; Moerner, W. *J. Am. Chem. Soc.* **2003**, *125*, 1174–1175.

54. Lord, S. J.; Conley, N. R.; Lee, H.-l. D.; Nishimura, S. Y.; Pomerantz, A. K.; Willets, K. A.; Lu, Z.; Wang, H.; Liu, N.; Samuel, R.; Weber, R.; Semyonov, A.; He, M.; Twieg, R. J.; Moerner, W. E. *ChemPhysChem* **2009**, *10*, 55–65.
55. Willets, K. A.; Callis, P. R.; Moerner, W. *J. Phys. Chem. B* **2004**, *108*, 10465–10473.
56. Sure, R.; Grimme, S. *J. Comput. Chem.* **2013**, *34*, 1672–1685.
57. Neese, F. *Wiley Interdiscip. Rev. Comput. Mol. Sci.* **2012**, *2*, 73–78.
58. Humphrey, W.; Dalke, A.; Schulten, K. *J. Mol. Graph. Model.* **1996**, *14*, 33–38.
59. Lord, S. J.; Lu, Z.; Wang, H.; Willets, K. A.; Schuck, P. J.; Lee, H.-l. D.; Nishimura, S. Y.; Twieg, R. J.; Moerner, W. *J. Phys. Chem. A* **2007**, *111*, 8934–8941.
60. Lu, Z.; Liu, N.; Lord, S. J.; Bunge, S. D.; Moerner, W.; Twieg, R. J. *Chem. Mater.* **2009**, *21*, 797–810.
61. Stsiapura, V. I.; Maskevich, A. A.; Tikhomirov, S. A.; Buganov, O. V. *J. Phys. Chem. A* **2010**, *114*, 8345–8350.
62. Ghosh, R.; Palit, D. K. *ChemPhysChem* **2014**, *15*, 4126–4131.
63. Alamiry, M. A.; Benniston, A. C.; Copley, G.; Elliott, K. J.; Harriman, A.; Stewart, B.; Zhi, Y.-G. *Chem. Mater.* **2008**, *20*, 4024–4032.
64. Zhang, W.; Lan, Z.; Sun, Z.; Gaffney, K. J. *J. Phys. Chem. B* **2012**, *116*, 11527–11536.
65. Förster, T.; Hoffmann, G. *Z. Phys. Chem.* **1971**, *75*, 63–76.
66. Jin, H.; Liang, M.; Arzhantsev, S.; Li, X.; Maroncelli, M. *J. Phys. Chem. B* **2010**, *114*, 7565–7578.
67. Law, K. *Photochem. Photobiol.* **1981**, *33*, 799–806.
68. Doolittle, A. K. *J. Appl. Phys.* **1952**, *23*, 236–239.
69. Zhou, F.; Shao, J.; Yang, Y.; Zhao, J.; Guo, H.; Li, X.; Ji, S.; Zhang, Z. *Eur. J. Org. Chem.* **2011**, *2011*, 4773–4787.
70. Massin, J.; Charaf-Eddin, A.; Appaix, F.; Bretonniere, Y.; Jacquemin, D.; Van Der Sanden, B.; Monnereau, C.; Andraud, C. *Chem. Sci.* **2013**, *4*, 2833–2843.
71. Suhina, T.; Amirjalayer, S.; Mennucci, B.; Woutersen, S.; Hilbers, M.; Bonn, D.; Brouwer, A. M. *J. Phys. Chem. Lett.* **2016**, *7*, 4285–4290.
72. Murarka, R. K.; Bhattacharyya, S.; Biswas, R.; Bagchi, B. *J. Chem. Phys.* **1999**, *110*, 7365–7375.